Orientation and Three-dimensional Organization of Actin Filaments in Dividing Cultured Cells

Douglas J. Fishkind and Yu-li Wang

Cell Biology Group, Worcester Foundation for Experimental Biology, Shrewsbury, Massachusetts 01545

Abstract. The current hypothesis of cytokinesis suggests that contractile forces in the cleavage furrow are generated by a circumferential band of actin filaments. However, relatively little is known about the global organization of actin filaments in dividing cells. To approach this problem we have used fluorescence-detected linear dichroism (FDLD) microscopy to measure filament orientation, and digital optical sectioning microscopy to perform three-dimensional reconstructions of dividing NRK cells stained with rhodamine–phalloidin. During metaphase, actin filaments in the equatorial region show a slight orientation along the spindle axis, while those in adjacent regions appear to be randomly distributed. Upon anaphase onset and through cytokinesis, the filaments become oriented along the equator in the furrow region, and along the spindle axis in adjacent regions. The degree of orientation appears to be dependent on cell–cell and cell–substrate adhesions. By performing digital optical sectioning microscopy on a highly spread NRK subclone, we show that actin filaments organize as a largely isotropic cortical meshwork in metaphase cells and convert into an anisotropic network shortly after anaphase onset, becoming more organized as cytokinesis proceeds. The conversion is most dramatic on the adhering ventral surface which shows little or no cleavage activity, and results in the formation of large bundles along the equator. On the dorsal surface, where cleavage occurs actively, actin filaments remain isotropic, showing only subtle alignment late in cytokinesis. In addition, stereo imaging has led to the discovery of a novel set of filaments that are associated with the cortex and traverse through the cytoplasm. Together, these studies provide important insights into the process of actin remodeling during cell division and point to possible additional mechanisms for force generation.

ACTIN and myosin undergo dramatic redistribution in cultured cells during the cell cycle (Fujiwara and Pollard, 1976, 1978; Aubin et al., 1979; Mittal et al., 1987; Sanger et al., 1989; Cao and Wang, 1990*a*,*b*). Their dynamic restructuring, from stress fibers in interphase cells to the cleavage furrow in dividing cells, is believed to be crucial for the generation of transient contractile forces for cell cleavage (for reviews see Mabuchi, 1986; Salmon, 1989; Satterwhite and Pollard, 1992; and references within Conrad and Schroeder, 1990). As for muscle contraction, it is hypothesized that cleavage forces are generated through a "sliding filament" mechanism involving the interaction and relative movement of a circumferential ring of actin and myosin filaments along the equator (Schroeder, 1970, 1972; Mabuchi, 1986; Satterwhite and Pollard, 1992). However, since nonmuscle cells lack a well-ordered sarcomeric structure, it has been difficult to precisely define the temporal and structural sequences leading to the formation of the contractile apparatus.

Much of the structural evidence for the "contractile-ring" model of cytokinesis comes from early EM studies of animal embryos and tissue culture cells, which show a submembranous band of anti-parallel microfilaments that appear to interdigitate with myosin-like minifilaments in the cleavage furrow (Schroeder, 1973; Sanger and Sanger, 1980). However, other studies indicate that the organization of cleavage furrow may be more complex. For example, some filaments within the furrow appear to lie at random angles to the equator (Opas and Soltynska, 1978; Zeligs and Wollman, 1979; Maupin and Pollard, 1986). In addition, polarization microscopy has shown a relatively weak birefringence in the cleavage furrow of dividing *Dictyostelium* amoeba, despite the presence of a concentrated band of actin filaments (Fukui and Inoué, 1991). Curiously, a second birefringent component is found to align along the spindle axis and colocalize with actin filaments, however the exact identity of molecules contributing to this signal remains unclear.

Given these diverse observations, it is critical to gain a more thorough understanding of the global orientation and three-dimensional organization of the actin cytoskeleton in dividing cells. In this study, we have used a combination of fluorescence-detected linear dichroism (FDLD)[1] and digital optical sectioning microscopy to examine cultured cells stained

1. *Abbreviations used in this paper*: FDLD, fluorescence-detected linear dichroism; IRM, interference reflectance microscopy.

with fluorescent phalloidin. FDLD microscopy is based on the differential absorption of plane-polarized light by fluorescent molecules as a function of orientation (Rost, 1991), and represents an extremely sensitive and specific method for defining the angular distribution of actin filaments (Kinoshita et al., 1991). Together with digital optical sectioning microscopy, a computational approach to remove out-of-focus fluorescence and generate high-resolution optical sections for three-dimensional analysis (Agard, 1984; Shaw and Rawlings, 1991), these methods can provide new information not easily obtained by conventional approaches.

Our results show that actin filaments undergo dynamic remodeling and reorientation during cytokinesis, with the extent of alignment appearing correlated with the degree of cell–cell and cell–substratum interactions. In addition, stereo renderings allow the first three-dimensional view of the unique spatial organization of actin filaments in dividing cells. Together, these results provide new insights into the restructuring of actin during cell division, and suggest that additional contractile mechanisms may operate during cytokinesis.

Materials and Methods

Cell Culture

The two normal rat kidney (NRK) cell clones used in this study (NRK-1, NRK-2) were subcloned from an NRK-52E stock obtained from American Type Culture Collection (Rockville, MD). Cells were cultured on glass coverslips at 37°C in 5% CO_2 for 48–72 h, using Kaighns modified F12 media (F12K, JRH Biosciences, Lenexa, KS) supplemented with 10% FBS (JRH Biosciences, Lenexa, KS), 1 mM L-glutamine, 50 μg/ml streptomycin, and 50 μg/ml penicillin.

Rhodamine-labeled Actin Paracrystals

Gel-filtered rabbit skeletal muscle actin was fluorescently labeled with tetramethylrhodamine-5-(6)-iodoacetamide (Molecular Probes, Inc., Eugene, OR) as previously described (Wang, 1984). The labeled actin had a molar dye to protein ratio of 1.03 using a molar extinct coefficient of 60,000 for rhodamine. Mg^{2+} paracrystals were produced by adding $MgCl_2$ (20 mM upon final dilution) to a 2.5 mg/ml stock of rhodamine–actin in 2 mM Tris-acetate, 50 μM $CaCl_2$, 0.1 mM ATP, and 0.1 mM DTT. Samples were diluted 1:50 with actin buffer containing 20 mM $MgCl_2$, mounted on a slide with coverslip, and then blotted to remove excess buffer and to compress the sample to alleviate movement of paracrystals during imaging.

Fixation and Labeling of Cells for F-actin and Mitotic Staging

Immediately before fixation, coverslips were briefly rinsed (30 s) with 37°C PBS, and then rapidly immersed into a glutaraldehyde-based fixative developed by Small et al. (1981, 1982) for ultrastructural preservation of actin filaments in tissue culture cells. Fixation conditions were 0.5% glutaraldehyde, 0.2% Triton X-100 in cytoskeleton buffer (137 mM NaCl, 5 mM KCl, 1.1 mM Na_2HPO_4, 0.4 mM KH_2PO_4, 2 mM $MgCl_2$, 2 mM EGTA, 5 mM Pipes, 5.5 mM glucose, pH 6.1) for 1 min at 22°C, followed by a brief rinse in cytoskeleton buffer, and then fixed for an additional 10 min in 1% glutaraldehyde in cytoskeleton buffer. Autofluorescence was quenched with 0.1% $NaBH_4$ for 5 min, and nonspecific binding was blocked for 1 h in PBS with 1% BSA. Cells were stained with 200 nM rhodamine-phalloidin (Molecular Probes, Inc.) and 100 ng/ml Hoechst 33258 (Sigma Chemical Co., St. Louis, MO) in PBS for 1 h, and then rinsed in PBS for an additional 30 min before examination. While the different lots of rhodamine-phalloidin used in this study gave identical results, we found the extent of FDLD can vary among lots and sources. More recent studies with bodipy phalloidin (Molecular Probes, Inc.) suggests it may be a less variable probe for FDLD imaging.

Fluorescence Microscopy and FDLD Measurements

Fluorescence images were acquired with a Zeiss Axiovert 10 (Carl Zeiss, Inc., Thornwood, NY) fitted with a rotatable specimen stage for sample orientation, a 40× Apochromatic (NA 1.0) objective with iris diaphragm for varying the numerical aperture and depth of field of the lens, and a Star-I cooled CCD camera (Photometrics, Tucson, AZ) linked to a Personal Iris 4D/20 computer workstation (Silicon Graphics Inc., Mountain View, CA) and image processor (Series 150; Imaging Technologies, Woburn, MA) for data storage, display, and mathematical operations. To preserve the geometric aspect of the displayed image, the pixel aspect ratio of CCD images was converted from 1:1 to 5:4 before input into the image processor which displays images as arrays of rectangular (5:4) pixels.

For FDLD imaging, 550-nm plane-polarized light was generated by passing a quartz-halogen source (Xenophot HLX, 12 V/100 W lamp; Osram, Germany) through a rotatable filter cassette containing (from source to sample): a visible-transmitting heat mirror (Oriel Corp., Stratford, CA), a 550-10 excitation filter (Ealing Electro-Optics, Inc., Holliston, MA), and linear polarizer (Oriel Corp.). The polarized light was then deflected to the sample using a filter cube containing a 565-DRLP dichroic beamsplitter and fluorescence was detected with a 590-DF-35 emission filter (Omega Optical, Inc., Brattleboro, VT). For all measurements, the objective was set to a numerical aperture of ~0.75 (assuming that the fluorescence intensity is proportional to the fourth power of the NA of the objective; Inoué, 1986), by closing the iris diaphragm down until the fluorescence intensity decreased to 31.6% of that obtained with the aperture fully open (i.e., NA 1.0). A schematic diagram of the instrumentation is shown in Fig. 1.

To obtain FDLD images, cells were oriented on the specimen stage so that the spindle axis, defined by the position of chromosomes, was aligned parallel to the horizontal axis of the display monitor. To insure accuracy, the camera (and thus display field) was never repositioned or altered during the course of the experiments. Samples were then illuminated with 550-nm plane-polarized light oriented parallel ($\parallel$) or perpendicular ($\perp$) to the spindle axis. These orientations minimize any depolarizing effect of the dichroic mirror. Pairs of $\parallel$ and $\perp$ images were then analyzed by generating differential images, i.e., ratios between the difference of the pair and the sum of the pair ($\parallel - \perp / \parallel + \perp$), following correction for the difference in excitation intensity at the two orientations. This correction factor was experimentally derived for our optics by imaging a mounted drop of 0.5 mg/ml rhodamine dye in glycerol at the two defined orientations and taking the ratio of the intensities. It should be noted that even with these precautions the values represent only a relative measure of the linear dichroism, since the purity of polarization can be significantly affected following passage through the objective lens (Axelrod, 1989) and structures on different planes are likely to make variable contributions to the measured value depending on the thickness of the sample relative to the depth of field.

The approximate mathematical relationship between the angular distribution of actin filaments and differential FDLD was derived as follows, assuming a two-dimensional structure:

$F_\parallel$ = fluorescence intensity with excitation light $\parallel$ to the equator.
$F_\perp$ = fluorescence intensity with excitation light $\perp$ to the equator.
$S_\parallel$ = cross section for absorption along the axis of each filament.
$S_\perp$ = cross section for absorption perpendicular to the axis of each filament.
$n(\theta)d\theta$ = number of filaments oriented at angle θ to $\theta + d\theta$.

Then:

$$F_\parallel \propto \int_0^{2\pi} n(\theta)\, S_\parallel \cos^2\theta\, d\theta + \int_0^{2\pi} n(\theta)\, S_\perp \sin^2\theta\, d\theta$$

$$F_\perp \propto \int_0^{2\pi} n(\theta)\, S_\parallel \sin^2\theta\, d\theta + \int_0^{2\pi} n(\theta)\, S_\perp \cos^2\theta\, d\theta$$

$$F_\parallel + F_\perp \propto \int_0^{2\pi} n(\theta) d\theta\, (S_\parallel + S_\perp) = N\,(S_\parallel + S_\perp)$$

$$F_\parallel - F_\perp \propto \left(\int_0^{2\pi} n(\theta)\, (\cos^2\theta - \sin^2\theta)\, d\theta\right)(S_\parallel - S_\perp)$$

$$\frac{F_\parallel - F_\perp}{F_\parallel + F_\perp} \propto \left[\frac{S_\parallel + S_\perp}{S_\parallel - S_\perp}\right] \int_0^{2\pi} \frac{n(\theta)}{N} (\cos^2\theta - \sin^2\theta)\, d\theta$$

where,

$$\int_0^{2\pi} \frac{n(\theta)}{N} (\cos^2\theta - \sin^2\theta)\, d\theta$$

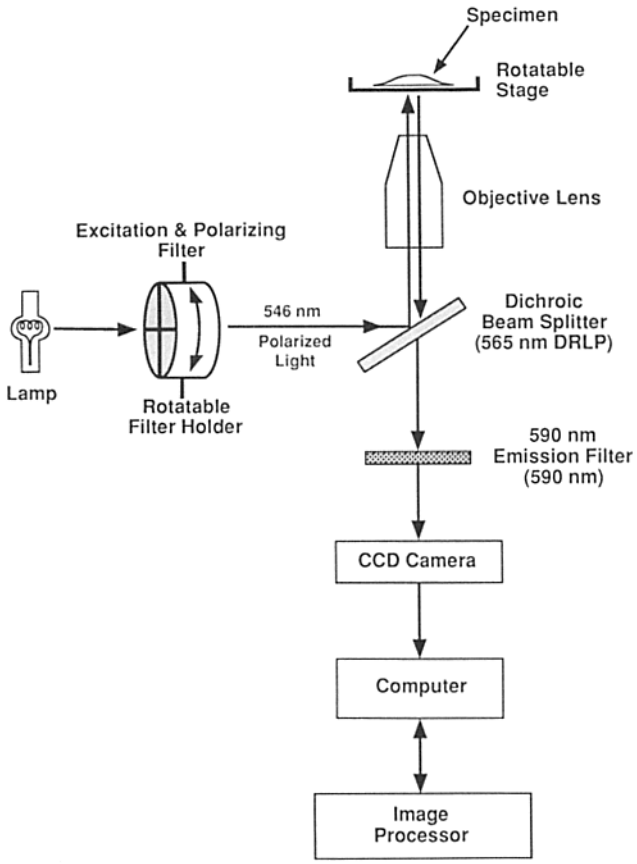

Figure 1. Diagram of instrumentation used for FDLD microscopy. Descriptions of the components are included in Materials and Methods. A differential FDLD image was produced from a pair of images acquired by illuminating the sample with plane-polarized light oriented first parallel and then perpendicular to the sample axis.

gives a weighted average angular filament distribution, with a weight equalling; +1 if oriented along the equator, 0 if oriented 45° to the equator, and −1 if oriented perpendicular to the equator. Therefore, a preferential orientation of actin filaments parallel or perpendicular to the spindle axis would give opposite signs for the FDLD value.

Images of FDLD were generated after proper scaling of the results, such that FDLD values in the range of −0.25 to 0.25 were mapped as gray values in the range of 0 to 255, with zero FDLD giving a display value of 128. In addition, to reduce the noise in FDLD images, the display value was set to zero if the intensity of a given pixel in either the ∥ and ⊥ images was below a value of two. The gray values were then displayed as "spectrum" pseudocolor, and hard copies were obtained using a UP7100MD color video printer (Sony Corp., Tokyo, Japan).

Quantification of the spatial and temporal changes in FDLD values were measured by averaging pixel values within a 2.5-μm-diameter spot (5 μm^2 area) positioned either in the center of the cell (i.e., at the equator), or in the subequatorial zone by moving the targeting spot along the x-axis to an area displaying the lowest FDLD value. Measurements were taken from cells at various stages of mitosis. Mitotic staging was determined from Hoechst staining of chromosomes, and represented only a relative estimate of the absolute stage of mitosis.

Conventional fluorescence imaging of rhodamine phalloidin (for F-actin) and Hoechst 33258 (for chromosomes) was performed with the system described above using epi-illumination from a second quartz-halogen lamp and Zeiss bandpass filter sets (#487915 for rhodamine and #487702 for Hoechst). Interference reflectance microscopy (IRM) was carried out as previously described (Cao et al., 1992).

Digital Optical Sectioning Microscopy and Three-dimensional Reconstructions

Rhodamine-phalloidin-stained cells were prepared as described above, and mounted in anti-photobleach reagent (Clark and Meyer, 1992) after the final rinse with PBS. A through focus series of optical sections were obtained using the Zeiss Axiovert 10, fitted with a computer-controlled stepping motor (0.28 or 0.65 μm step size), a 100× (1.3 NA) Neofluar objective, and a rhodamine filter set (#487915). The images were collected from a small region in the center of the field to limit spherical aberration. Digital images acquired with the cooled CCD camera were stored as disk files in the Iris 4D/20 workstation. Removal of out-of-focus fluorescence and restoration of optical slices were achieved using the nearest neighbor algorithm (Castleman 1979; Agard, 1984; Shaw and Rawlings, 1991) and point spread functions obtained with our optical system. Examination of deconvolved images of fluorescent beads indicates a resolution along the z-axis of ~0.7 μm.

Three-dimensional reconstructions of x–y stereo pairs were produced by stacking a set of deconvolved sections and projecting them at angles +10° and −10° from the optical axis using custom generated software. To produce cross-sectional stereo views of filaments in the furrow region (i.e., a y–z perspective allowing a side view of the furrow region from the subequatorial border), a 5 × 30-μm boxed area of just the cleavage furrow zone was used for reconstruction and the image stack was viewed at an altitude angle of 3° and azimuth angles of +2.5° and −2.5° (see Fig. 8 *d*). The aspect ratio was maintained and the space between optical slices was filled by linear interpolation. Direct examination and analysis of three-dimensional data sets were performed by displaying red–green stereo pairs on the monitor. For additional three-dimensional analysis, a series of stereo pairs at different angles were viewed as three-dimensional movie loops, aiding in the assessment and evaluation of complex three-dimensional structures within the cell.

Results

FDLD Imaging of Rhodamine-labeled Actin Filament Bundles

To test the application of FDLD imaging in determining the preferred orientation of actin filaments, we first examined Mg^{2+} paracrystals of rhodamine-labeled actin. The fluorescence intensity appeared slightly higher with excitation light polarized parallel to the bundles than with light polarized perpendicular to the bundles (Fig. 2, *a* and *b*). However, when the differential FDLD image was calculated (see Materials and Methods), striking contrast, reflecting opposite signs of the differential FDLD values, was obtained for the two populations of orthogonal bundles (Fig. 2, *c* and *d*). Paracrystals oriented 45° to either axis appeared neutral (*green*) in the differential FDLD image (Fig. 2, *c* and *d*). This observation is consistent with the dependence of FDLD on a weighted average of the angular distribution of filaments (see Materials and Methods), with those at 45° making no contribution to the differential value.

Since FDLD is highly sensitive to the rigidity and orientation of the fluorescent probe associated with the target structure, we next asked whether a similar technique can be applied to phalloidin-labeled filaments by examining cultured interphase cells stained with rhodamine–phalloidin. To ensure a high-degree of cytoskeletal integrity, cells were fixed with a glutaraldehyde-based fixative known to preserve labile structures such as the lamellipodia (Small et al., 1981, 1982). As shown in Fig. 3, stress fibers emitted intense fluorescence when illuminated with light oriented parallel to the axis of the fiber (Fig. 3 *a*), and reduced fluorescence with light perpendicular to the axis (Fig. 3 *b*). Differential FDLD imaging showed opposite signs, as depicted in red and blue,

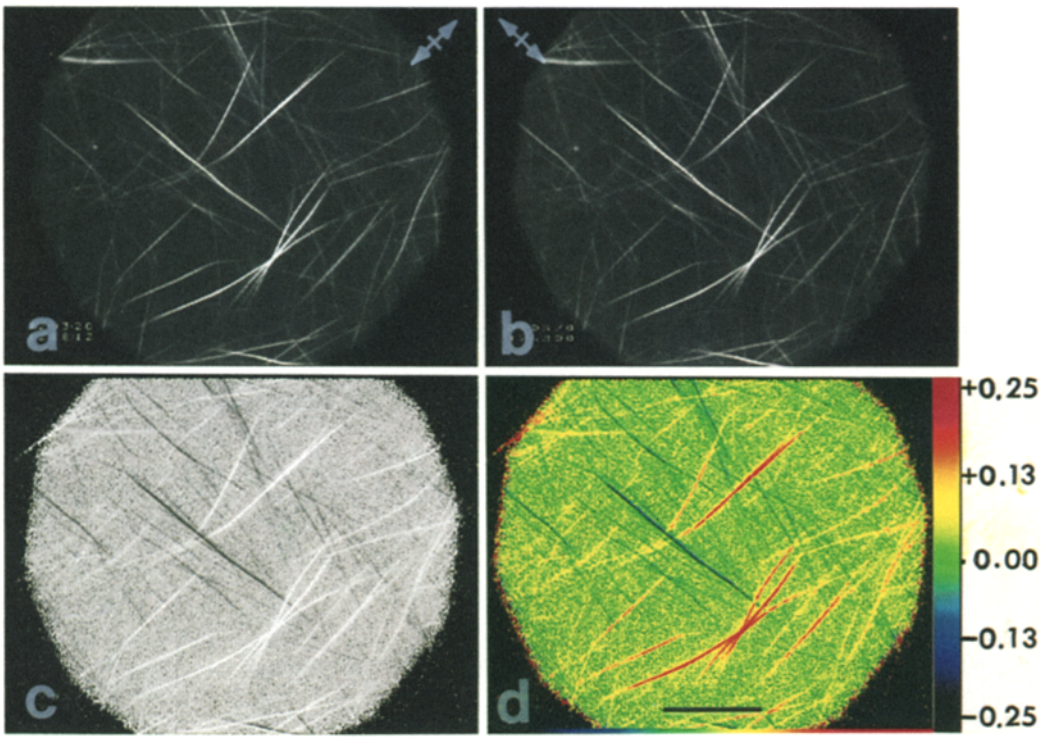

Figure 2. FDLD imaging of Mg^{2+}-paracrystals of rhodamine-labeled actin filaments. Images were acquired with plane-polarized light oriented along two orthogonal directions (*a* and *b*) as indicated by the vector symbols in the upper corner of the images (*arrows*). Differential FDLD images were then calculated and displayed either in grayscale values (*c*) or as a pseudo-color image (*d*). Actin bundles show a slightly higher intensity in direct images when oriented parallel to the plane of polarization (*a* and *b*). The effect is greatly amplified in differential FDLD images, with bundles lying along the two orthogonal directions showing opposite signs of FDLD values. The color bar in *d* represents the standard relationship between FDLD values and color applied to the 0–255 display values, and may be referred to for analysis of any FDLD images presented in the paper. Bar, 25 μm.

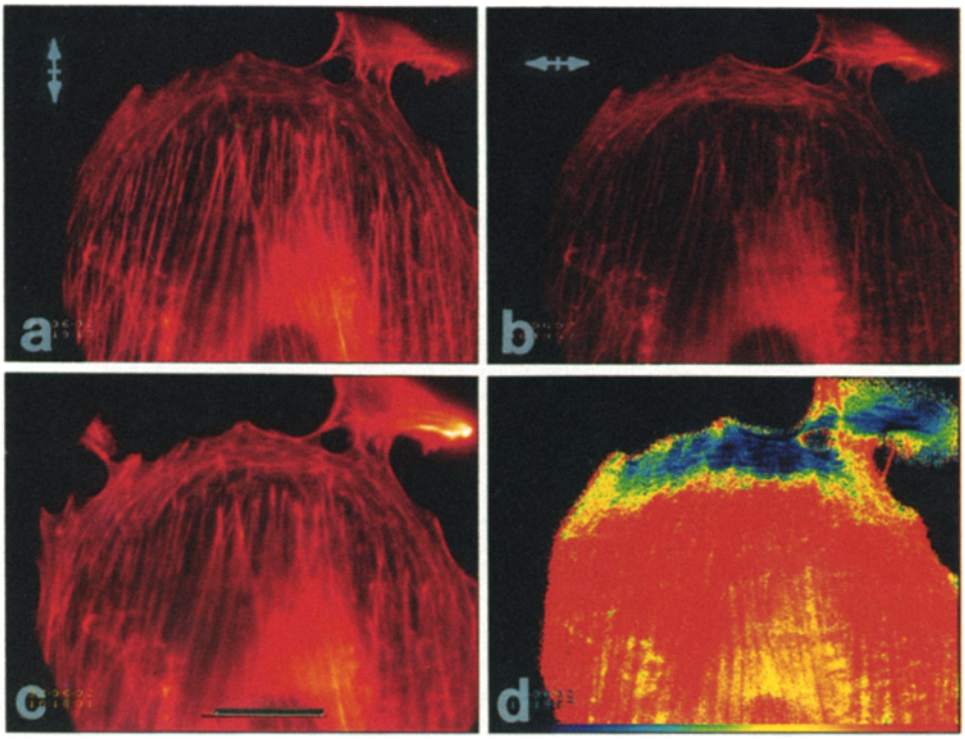

Figure 3. FDLD imaging of actin filaments in an interphase NRK cell stained with rhodamine-phalloidin. Fluorescence images were obtained using plane-polarized excitation light oriented parallel (*a*) or perpendicular (*b*) to the long axis of the cell as indicated by the vector symbols (*arrows*). Corresponding conventional fluorescence image is shown in *c*. The differential FDLD image (*d*) is displayed in pseudo-color using the same mapping as in Fig. 2. Stress fibers show strong positive values owing to their alignment along the long axis of the cell. Actin "arcs" in the lamella lie along a perpendicular direction and show negative values. Bar, 20 μm.

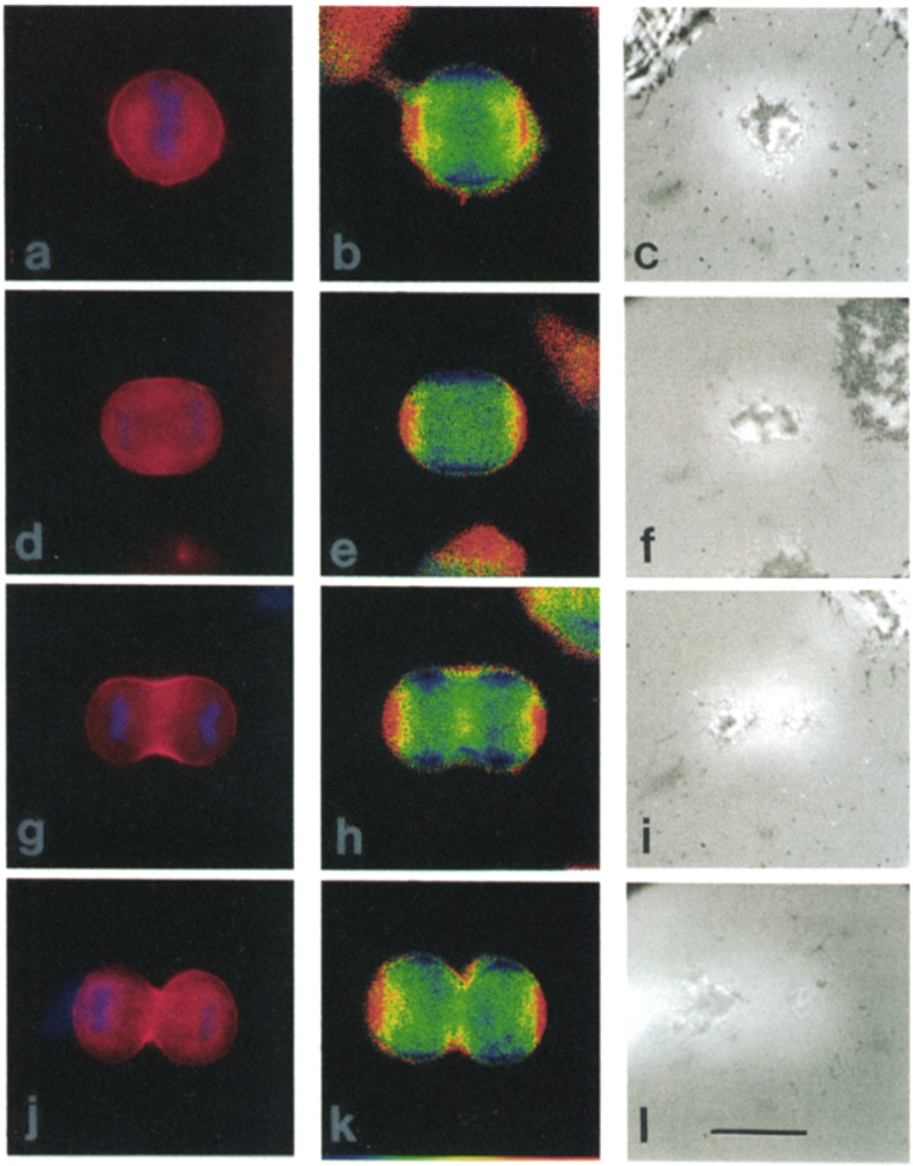

Figure 4. FDLD imaging of actin filaments in dividing NRK-1 cells stained with rhodamine–phalloidin. Conventional fluorescence images of rhodamine–phalloidin and Hoechst-33258 staining of cells at metaphase (*a*), early anaphase (*d*), late anaphase (*g*), and telophase (*j*), show the overall distribution of F-actin and chromosomes. Corresponding differential FDLD images are shown in the middle column (*b*, *e*, *h*, and *k*) and IRM images are shown in the right-hand column (*c*, *f*, *i*, and *l*). FDLD imaging indicates that at metaphase and early anaphase, there is no strong preferred orientation of actin filaments except for an apparent alignment of filaments parallel to the spindle axis in the equatorial region of the cell (*b* and *e*, *bluish-green striations*). During cytokinesis, the furrow region shows only a slight alignment of actin filaments along the equator (*h* and *k*, *yellow-green band*), while adjacent regions show a more pronounced alignment along the spindle axis (*h* and *k*, *bluish-green sub-equatorial bands*). The strong positive (*red*) and negative (*purple*) differential FDLD values along the edge is an optical effect due to the spherical shape of dividing NRK-1 cells and the concentration of actin filaments along the cortex. IRM images indicate that NRK-1 cells remain attached to the coverslip through weak adhesions near the equator during metaphase (*c*) and early anaphase (*f*), and under the forming daughter cells later in cytokinesis (*i* and *l*). Bar, 15 μm.

between stress fibers and actin "arcs" that were localized behind the leading edge and oriented perpendicular to stress fibers (Fig. 3 *d*). For the sake of consistency, filament orientation in the y direction will be shown in red and that in the x direction will be shown in blue throughout the rest of this study.

Orientation of Actin Filaments in Dividing NRK Cells

We then used FDLD imaging to determine the preferred orientation of actin filaments in dividing cells stained with rhodamine–phalloidin at different stages of mitosis. NRK-1 cells underwent rounding upon entry into mitosis and formed the classic dumb-bell shape, typical of less adherent dividing cells that retain only limited adherence to the coverslip during cytokinesis (Fig. 4). At metaphase and during early anaphase, FDLD images showed a preferential alignment of actin filaments along the spindle axis in the equatorial region (Fig. 4, *b*, *e*; *blue-green* equatorial zone). The edge of the cell showed opposite signs of differential FDLD in polar and equatorial regions, as expected for cortical filaments that lie along the cell surface. Upon initiation of cell cleavage, actin filaments in the furrow region became slightly oriented parallel to the equator (Fig. 4 *h*; *yellow-green equatorial zone*), whereas those in adjacent regions were preferentially aligned along the spindle axis (Fig. 4 *h*; *blue-green sub-equatorial bands*). This pattern of orientation persisted through cytokinesis (Fig. 4 *k*).

The interpretation of FDLD images from NRK-1 cells is limited by both the spatial resolution and the relatively large thickness of this clone. We therefore performed similar measurements with a more adhesive subclone of NRK cells (NRK-2), which remained well-spread during cell division due to increased cell–cell and cell–substratum interactions (Fig. 5). Live video recordings of well-spread NRK-2 cells consistently showed that lateral cell borders remained attached to neighboring cells without undergoing significant constriction during the progression through karyokinesis and cytokinesis (data not shown), a result indicative of asymmet-

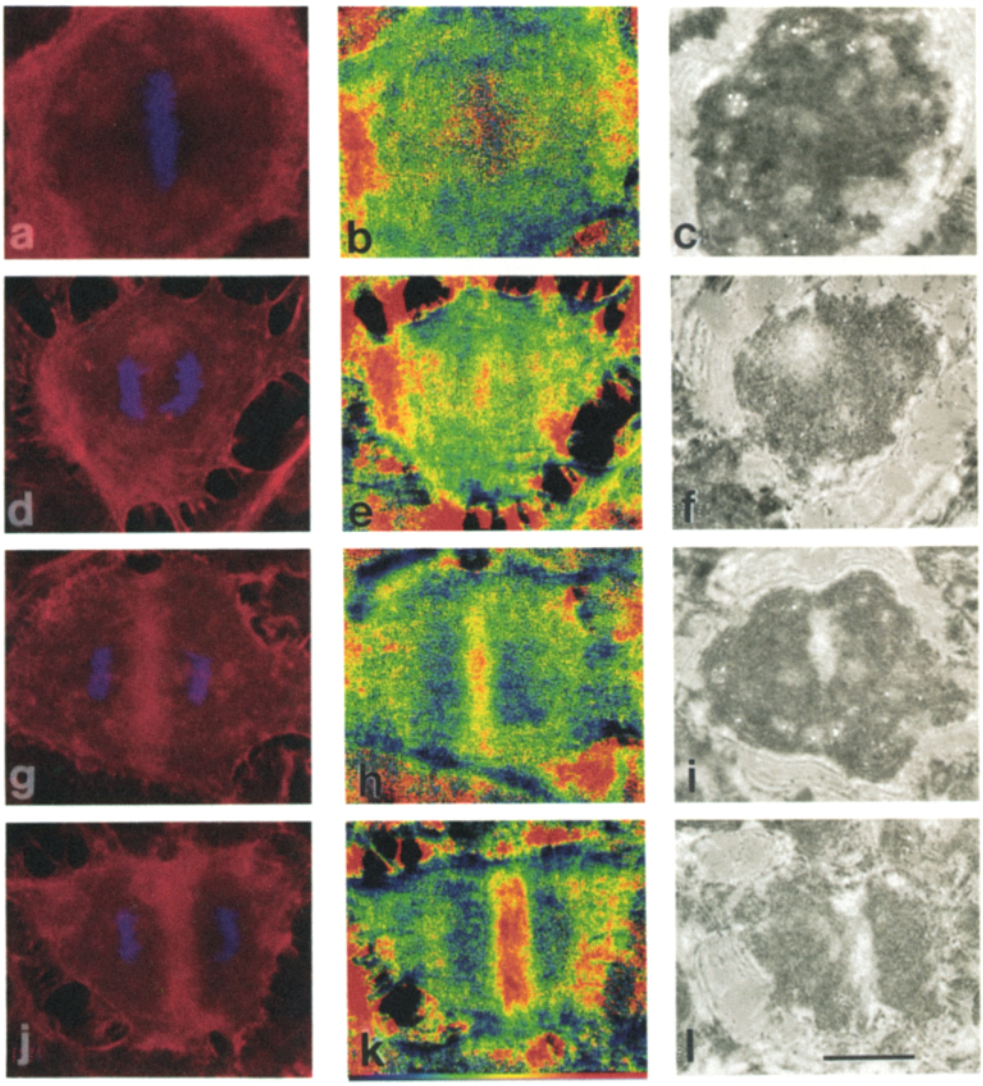

Figure 5. FDLD imaging of actin filaments in dividing NRK-2 cells stained with rhodamine–phalloidin. Conventional fluorescence images of rhodamine phalloidin and Hoechst-33258 staining of cells at metaphase (*a*), early anaphase (*d*), late anaphase (*g*), and telophase (*j*), show the overall distribution of F-actin and chromosomes. Corresponding differential FDLD images are shown in the middle column (*b*, *e*, *h*, and *k*) and IRM images are shown in the right-hand column (*c*, *f*, *i*, and *l*). FDLD imaging indicates that at metaphase there is no strong preferred orientation of actin filaments (*b*, *green hue*), except for slight alignment along the spindle axis near the equator. However, upon anaphase onset and throughout telophase actin filaments undergo a dramatic reorganization, showing strong alignment of filaments parallel to the equator in the furrow region (*e*, *h*, and *k*, *yellow-red band*), and strong alignment along the spindle axis in adjacent regions (*e*, *h*, and *k*, *bluish subequatorial bands*). Conventional fluorescence and IRM images suggest that NRK-2 cells maintain a well-spread morphology due to strong cell–cell and cell–substrate adhesion during cell division. Bar, 15 μm.

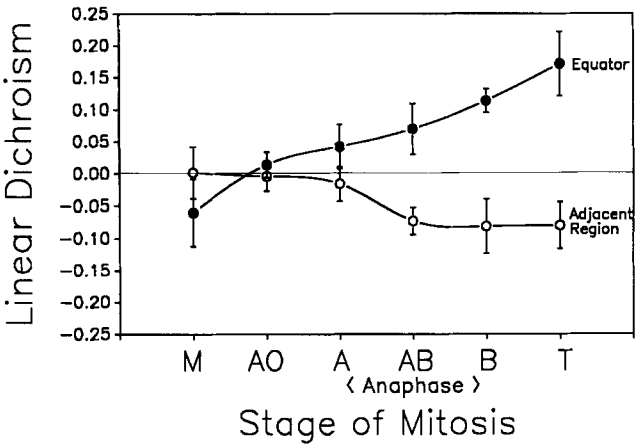

Figure 6. Differential FDLD analysis of the temporal development of filament alignment at the equator (●) and adjacent regions (○) in dividing NRK-2 cells. At the equator, differential FDLD values rise from slightly negative values at metaphase to positive values following anaphase onset, reflecting the strong parallel alignment of filaments along the equator. In contrast, values in adjacent regions fall from neutral during metaphase and early anaphase, to negative values reflecting the strong axial alignment of filaments. *M*, Metaphase (n = 13); *AO*, Anaphase Onset (n = 8); *A*, Anaphase-A (n = 7); *AB*, Anaphase-AB (n = 11); *B*, Anaphase-B (n = 6); *T*, Telophase (n = 4).

ric cell cleavages (see Fig. 8 below for three-dimensional views). Moreover, the flattened morphology of NRK-2 cells did not appear to significantly affect the efficiency of cell division, as evidenced by the observation that long-term cultures of NRK-1 and NRK-2 cells contained approximately the same frequency of bi- and multi-nucleated cells (i.e., 1.8% versus 2.1%, respectively).

At metaphase, NRK-2 cells generally displayed little preferred orientation of actin filaments, except for slightly negative values detected in the equatorial region (Figs. 5 *b* and 6). While suggestive of filament orientation along the spindle axis, observations in this region are limited by a relatively

low signal to noise ratio and should therefore be interpreted cautiously. Upon anaphase onset and progressively through cytokinesis, actin filaments underwent a dramatic reorganization, showing increased alignment parallel to the equator in the furrow region (Fig. 5, *e*, *h*, and *k*; *yellow–red equatorial band*) and along the spindle axis in regions immediately adjacent to the furrow (Fig. 5, *e*, *h*, and *k*; *blue–purple subequatorial bands*). Careful analysis of the temporal and spatial changes from a number of cells indicated that differential FDLD at the equator rose from slightly negative values at metaphase to positive values following anaphase onset (Fig. 6; *closed circles*). In contrast, differential FDLD in the region adjacent to the equator fell from neutral values at metaphase and early anaphase to more negative values during the later stages of cell division (Fig. 6, *open circles*).

Digital Optical Sectioning Microscopy and Three-dimensional Analysis of Actin Filaments in Dividing Cells

To attempt to directly image the distribution of actin filaments contributing to the FDLD signals and to compare the distribution of filaments on different focal planes, we examined phalloidin-stained cells using digital optical sectioning microscopy. These studies were carried out primarily with

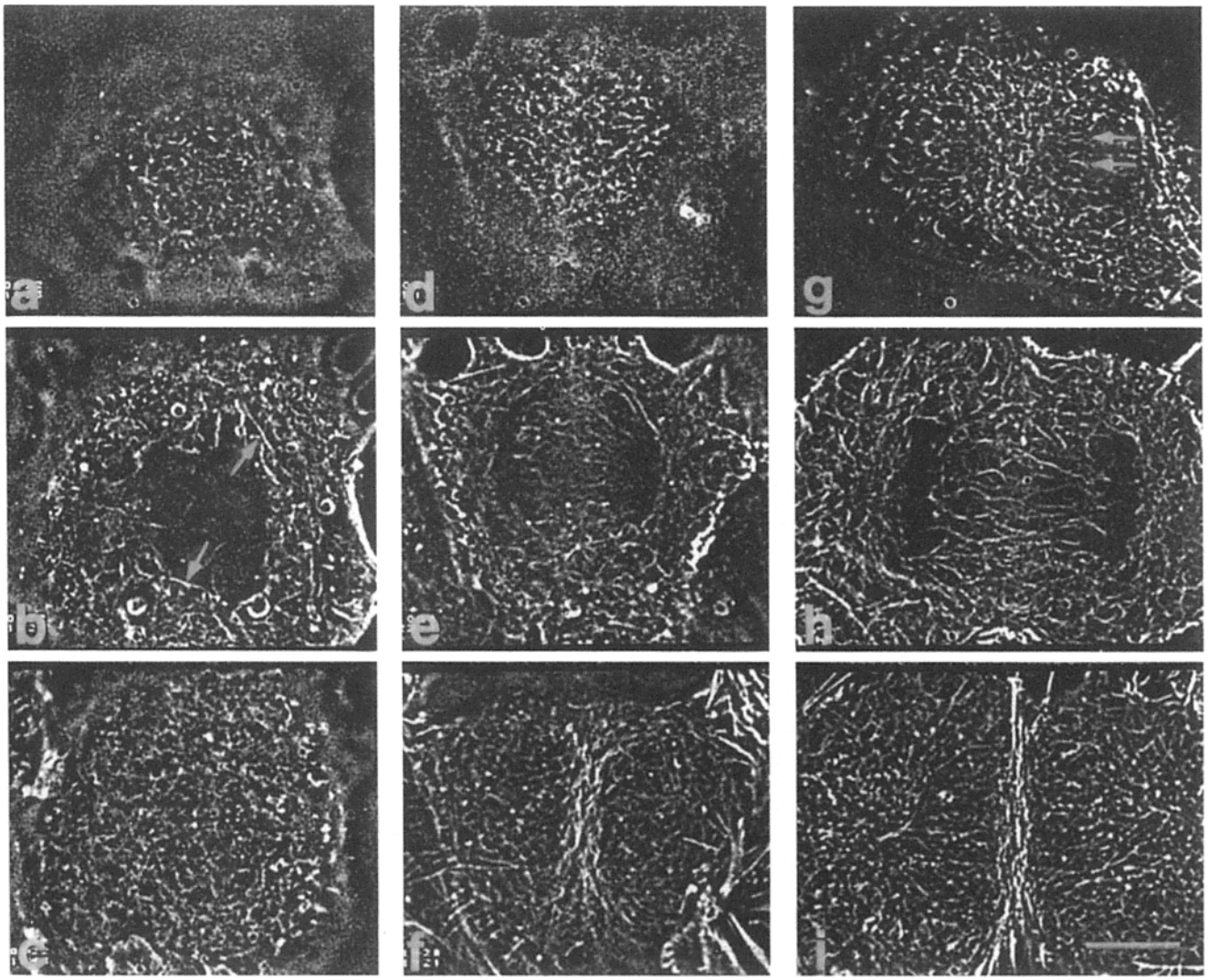

Figure 7. Digital optical sectioning microscopy of adherent NRK-2 cells stained with rhodamine–phalloidin during cell division. Optical sections were collected at early anaphase (*a–c*), mid-anaphase (*d–f*), and telophase (*g–i*), through the top (*a*, *d*, and *g*), middle (*b*, *e*, and *h*), and bottom (*c*, *f*, and *i*) portion of each cell. During early anaphase, filaments appear randomly distributed on the top and bottom surfaces (*a* and *c*), as well as within the cytoplasm (except for those in close apposition to the spindle) (*b*, *arrows*). However, later in anaphase, filaments along the ventral surface become more strongly aligned parallel to the equator (*f*), while filaments on the dorsal surface remain randomly organized (*d*). Note that centrally localized filaments show indications of alignment parallel to the spindle axis (*e*), and become progressively more ordered later in telophase (*h*). During cytokinesis, filaments on the dorsal "cleaving" surface appear as a dense meshwork that converge at the equator, with many filaments in sub-equatorial regions oriented along the spindle axis (*g*, *arrows*). In contrast, along the ventral adhering surface, filaments in the equatorial region are strongly aligned parallel to the equator. Those outside of the furrow are oriented along the spindle axis. Bar, 10 μm.

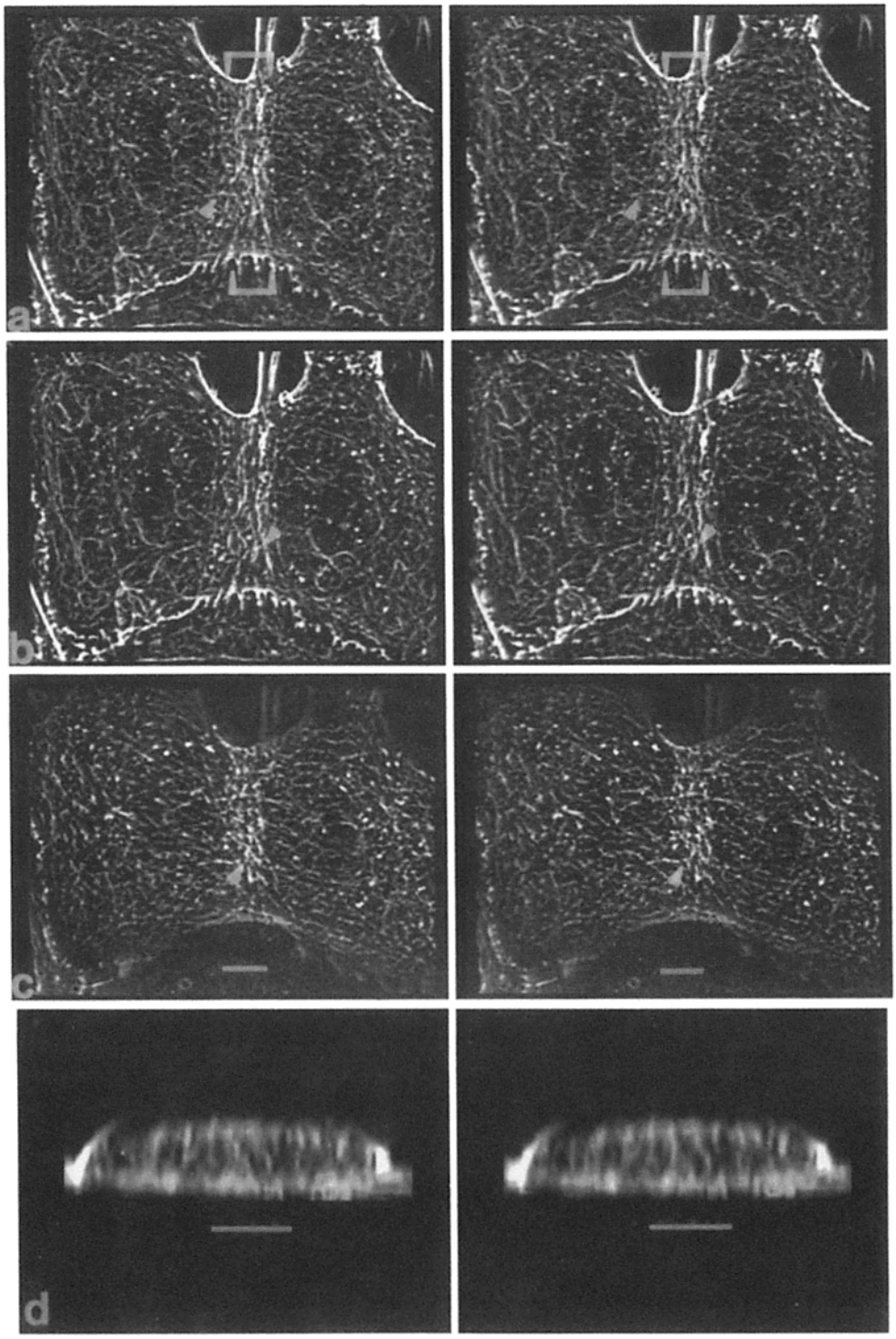

Figure 8. Stereo images of the three-dimensional organization of F-actin in a dividing NRK-2 cell at telophase, showing; *a*, complete x–y view of the cell using all optical sections; *b*, bottom-half x–y view of the cell; *c*, top-half x–y view of the cell; and *d*, cross-sectional, cutaway y–z view of only the cleavage furrow region (see Materials and Methods for the generation of this perspective). The brackets in panel a define the 5 × 30-μm box used to reconstruct the cross-sectional y–z rendering of the furrow region in *d*. All 18 deconvolved optical slices (0.275 μm step/section) were used to generate the complete and cross-sectional views (*a* and *d*), while the bottom (*b*) and top (*c*) halves were generated with sections 1–9 and 10–18 of the series, respectively. The bottom (*b*) and top (*c*) views are projected from the inside of the cell at a level mid-way through the spindle. The y–z cutaway view of the cleavage furrow (*d*) is projected from the side, such that the upper boundary of the image corresponds to the top (dorsal) surface of the furrow and the lower boundary to the bottom (ventral) surface. Note, that a number of actin filaments appear to project into the cell interior at various angles from the dorsal and ventral cortical surfaces (*arrowheads*). *a–c* are all displayed at the same magnification. Bars, 5 μm.

the well-spread NRK-2 cells, due to their exceptional optical properties. At metaphase, actin filaments were present as apparently isotropic networks on both the top "dorsal" and bottom "ventral" cortical surfaces of the cell (Fig. 7, *a* and *c*). Filaments were also observed in the interior cytoplasm, often in close apposition to the spindle (Fig. 7 *b*, *arrows*). By anaphase, filaments on the top cortex were still randomly distributed (Fig. 7 *d*), however cytoplasmic filaments appeared more aligned along the spindle axis (Fig. 7 *e*). In addition, filaments along the ventral surface were concentrated at the equator and showed strong equatorial alignment (Fig. 7 *f*). By telophase, a meshwork of actin filaments had formed along the equator of the dorsal cortex, and some filaments in adjacent regions were observed to lie parallel to the spindle axis (Fig. 7 *g*, *arrows*). In central regions, many actin filaments remained aligned parallel to the spindle axis (Fig. 7 *h*). As with anaphase, strong alignment along the equator was localized on the ventral surface, with some filaments in adjacent regions lying parallel to the spindle axis (Fig. 7 *i*).

To examine the three-dimensional arrangement of these

filament arrays, stereo pairs of images were produced from either complete or partial stacks of deconvolved optical slices of dividing cells (Fig. 8). Of 51 cells examined, all showed the representative features described here. From complete reconstructions, it was clear that furrow ingression occurred primarily from the top surface, allowing a direct comparison between actin organization along the dorsal surface that underwent active cleavage and ventral surface that showed little or no cleavage activity due to cell-substratum adhesion (Fig. 8 *a*).

Careful analysis showed that highly aligned equatorial filaments were largely restricted to the noncleaving ventral surface and lower lateral margins of the equator (Fig. 8, *a* and *b*), whereas the cleaving dorsal surface and the upper lateral margins of the equator were associated with a less ordered network of filaments (Fig. 8, *a* and *c*). Most interestingly, stereo renderings of optical stacks revealed an additional set of filaments that traversed through the central region of the cell (Fig. 8, *a–c*, *arrows*). Many of these filaments appeared to originate from discrete sites on the dorsal and ventral cortex and project into the cell at various angles. In some cases the filaments appeared to traverse the entire distance between dorsal and ventral surfaces (Fig. 8 *a*, *arrow*). These filaments were most easily observed in cross-sectional, cut away stereo views of the cleavage furrow region, where they appeared to form a network of interlaced projections emanating from the cortical surfaces of the furrow (Fig. 8 *d*, see Materials and Methods for generation of this perspective). While the imaging of such projections are limited by the z resolution of the microscope and linear interpolation of data, the continuity along filaments lying at variable angles suggests they represent true structures rather than artifacts of mathematical operations.

Discussion

Cell movements such as lamellipodial extension and cleavage furrow contraction rely heavily on dynamic remodeling of the actin cytoskeleton. Due to the transient and complex nature of actin filament networks, it has been difficult to define the global organization of the actin cytoskeleton before and during these events using conventional microscopic techniques. In this study, we have applied FDLD and digital optical sectioning microscopy, which offer complementing advantages, to analyze the temporal and spatial reorganization of actin filaments in dividing cells. FDLD microscopy provides a relative measure of the two-dimensional orientation of actin filaments, and is capable of detecting a small degree of order within an otherwise randomly organized structure. In contrast, digital optical sectioning microscopy provides high-resolution, three-dimensional images of the organization of actin filaments, however its information is usually qualitative in nature and minor degrees of order can be difficult to perceive.

Despite these differences, the two approaches have yielded consistent results regarding the organization of actin in dividing cells. Both indicate that actin filaments undergo dramatic restructuring from a fairly isotropic state in metaphase to a more highly ordered state during later stages of cell division (Figs. 4–7). While similar observations were made with two morphologically distinct subclones of NRK cells, the reorganization of actin was best observed in the more adherent NRK-2 cells, where a progressive increase in filament alignment occurs both along the equator and parallel to the spindle axis (Figs. 5 and 6). Dramatic restructuring was initiated shortly after anaphase onset and intensified throughout anaphase and telophase, correlating well with the time course of tension development observed in other systems. For example, as shown by Usui and Yoneda (1982), cortical tension in sea urchin embryos begins to rise immediately after anaphase onset, concurrent with the initiation and restructuring of an isotropic meshwork of microfilaments into filament bundles in the equator. A similar reorganization of actin filaments observed in dividing *Dictyostelium* amoeba (Kitanishi-Yumura and Fukui, 1989), was accompanied by the appearance of a strong positive birefringence along the spindle axis and a weaker birefringence along the equator (Fukui and Inoué, 1991).

Longitudinal Filaments in Cell Division

Interestingly, the earliest detectable orientation of actin filaments was along the spindle axis in metaphase cells (Figs. 4–6), suggesting that forces (or torques) may be exerted on actin filaments along the longitudinal direction. For both NRK-1 and NRK-2 subclones, the orientation becomes progressively stronger and appears to extend for considerable distances beyond the equator during later stages of cell division (Figs. 4–6). Although longitudinal filaments have been previously observed in dividing spermatocytes (Forer and Behnke, 1972; LaFountain et al., 1992), epithelial cells (Zeligs and Wollman, 1979), tissue culture cells (Sanger, 1975; McDonald, 1984; Maupin and Pollard, 1986), embryos (Opas and Soltynska, 1980), amoeba (Fukui and Inoué, 1991), and higher plant cells (Molè-Bajer et al., 1988), this component has received little attention within the context of the contractile ring hypothesis which emphasizes the importance of filaments lying along the equator.

One possible cause of the longitudinal alignment is the ingression of the equator, which may exert tension on the neighboring cortex and cause passive alignment of filaments (Arnold, 1976). However, this appears unlikely given the early appearance of longitudinal filaments before the appearance of the cleavage furrow. A second possibility is that these filaments may be in the process of recruitment to the cleavage furrow along longitudinal paths, as previously shown by Cao and Wang (1990*b*). Our results with digital optical sectioning microscopy indicate that the longitudinal orientation is present not only on the cortex, but throughout the cytoplasm where filaments appear aligned within the spindle (Fig. 7). This latter finding may be due to passive alignment by entrapment or binding to components of the spindle apparatus as previously proposed (Maupin and Pollard, 1986; Molè-Bajer et al., 1988). Alternatively, it is possible that the spindle may play an active role in orienting cortical and cytoplasmic actin filaments, and establishing a bipolar flow of cytoskeletal elements in dividing cells (Bray and White, 1988; Hird and White, 1993). Such interactions between the spindle and actin cytoskeleton, potentially mediated by members of the growing family of motor proteins involved in mitosis and cytokinesis (Skoufias and Scholey, 1993), could provide a mechanical signal involved in establishing the position of the cleavage furrow (Rappaport, 1986; Mabuchi, 1986; Margolis and Andreassen, 1993).

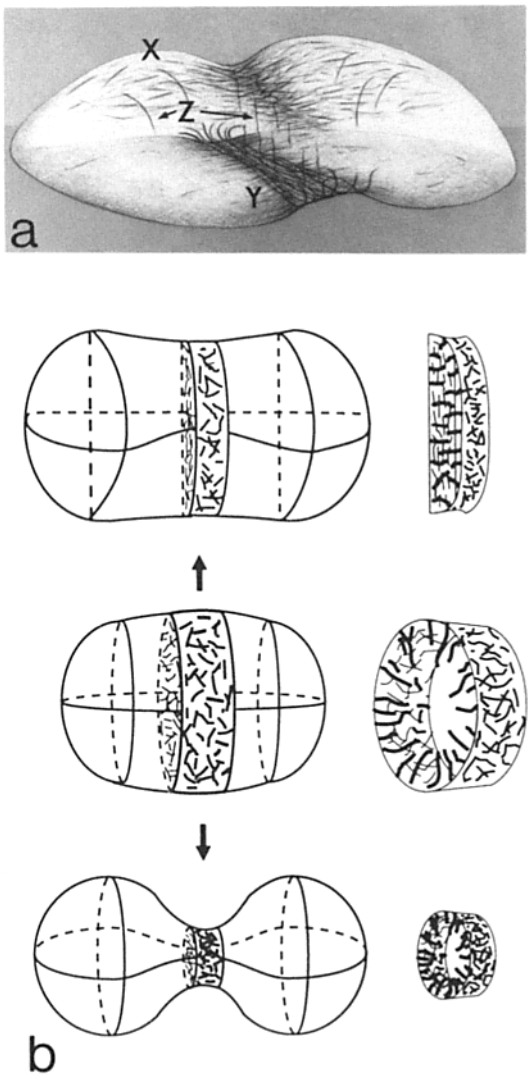

Figure 9. Schematic representation of the organization of cortical-associated actin filaments in a dividing NRK-2 cell (*a*), and a hypothetical model for cytokinesis involving three-dimensional, isotropic contractile forces (*b*). The schematic in *a* shows the organization of three spatially distinct arrays of filaments, including the cortical meshwork of longitudinal and equatorial filaments on the cleaving dorsal surface (*x*), the strongly aligned filaments on the ventral noncleaving surface (*y*), and cortically associated traversing filaments projecting from the dorsal and ventral surfaces into the cell interior (z). The isotropic contraction model for cytokinesis (*b*) proposes that forces are transmitted in all directions by a three-dimensional network of filaments in the equatorial region (*middle cell*), resulting in the shrinkage and ingression of the cleavage furrow at the equator (*top* and *bottom cells*). The actual pattern of cell cleavage is modulated by resistive forces such as cell–cell and cell–substratum adhesion. Thus, with minimal adhesive resistance, the cell cleaves symmetrically and cortical actin filaments show limited preferred orientation (*bottom cell*). However, with strong resistance near the ventral surface, cell ingression is limited to the dorsal surface, while ventral actin filaments show a high degree of equatorial alignment due to anisotropic resistive forces (*top cell*). Cross-sectional views of the equatorial regions (*right*) are provided to show the shape of the furrow region and three-dimensional organization of actin filaments under these conditions.

Equatorial Filaments in Cell Division

Consistent with the current model of cytokinesis, both subclones of NRK cells show a preferential equatorial orientation of actin filaments in the region of cell cleavage. However, it is also clear from digital optical sectioning microscopy that the spatial organization of actin in the cleavage furrow is far more complex than a simple circumferential band of equatorial filaments (Figs. 7 and 8). Strong equatorial alignment of actin filaments appear to concentrate along the noncleaving ventral cortex of NRK-2 cells, while filaments in the actively cleaving dorsal cortex are present as less-ordered meshworks (Figs. 7 and 8).

One possible explanation for variable degrees of equatorial alignment is that the assembly of contractile structures may respond to the actual requirement of force needed for cytokinesis. Thus, the equatorial alignment on the ventral cortex may be amplified by the attempt of cells to overcome the strong cell–cell and cell–substratum adhesions, while cleavage on the nonresistive dorsal cortex can be accomplished with a minimal degree of equatorial organization (Figs. 7 and 8). This kind of mechanical feedback has been indicated in the smooth muscle system, where the extent of myosin light chain phosphorylation increases under increased resistance to contraction (Hai and Szeto, 1992). In addition, it may explain the variability of filament alignment in different cell types during cytokinesis. For example, resistive forces may be quite high during early cleavages of large embryos, causing significant equatorial alignment of filaments in the furrow (Perry et al., 1971; Arnold, 1976). Similarly, excess resistance may account for the dramatic organization of filaments in dividing cells under the constraints of agar overlay (Yumura et al., 1984; Kitanishi-Yumura and Fukui, 1989; Fukui and Inoué, 1991) or in cleavage furrows isolated from embryos attached to charged-coated surfaces (Yonemura and Kinoshita, 1986). On the other hand, resistive forces on poorly adherent cells are likely to be low, which may account for the limited degree of filament alignment observed in NRK-1 cells (Fig. 4), and less-ordered arrays of filaments reported in the cleavage furrow of HeLa cells (e.g., Fig. 5 in Maupin and Pollard, 1986).

A second idea is that the equatorial alignment is not actively assembled for cytokinesis, but is rather a passive consequence of anisotropic counter forces applied to the cortex (Rappaport, 1991). Such counter forces could likely arise from strong cell–cell and cell–substratum adhesion, resisting the contractile activity for cell cleavage. This explanation implies that an alternative mechanism, other than the contraction of a purse string, may be responsible for ingression of the cell surface.

Possible Forces Involved in Cytokinesis

The results from this study indicate that the actin scaffolding of dividing cells is composed of a complex three-dimensional network of filaments, rather than a simple circumferential ring (Fig. 9). Assuming that actin filaments provide a structural framework for the action of myosin-based motors and that the orientation of actin filaments reflects the direction of forces, we speculate that longitudinal and equatorial fibers, together with filaments projecting into the cytoplasm could provide three-dimensional forces to effect cell cleavage (Fig. 9 *a*).

One may consider specific contributions of these force components to cytokinesis. First, the cortical filament meshwork could transmit isotropic contractile forces in the equatorial region, causing a shortening along both the equator and spindle axis (Fig. 9 *b*). In addition, the traversing filaments could transmit forces perpendicular to the cell surface, resulting in a direct ingression of the cell surface. The actual pattern of cell cleavage will be determined by a balance of these forces in relation to adhesive and/or internal resistive forces, such that ingression occurs actively in regions where contractile forces exceed resistive forces. This provides a plausible explanation for why nonadhering cells undergo symmetric cleavages with a low degree of filament ordering, while highly adhesive cells display asymmetric cleavages with more ordered structures. Given the apparent structural complexity of the contractile apparatus of dividing cells and the diversity of cell cleavages found in nature (Beams and Kessel, 1976; Zeligs and Wollman, 1981; Ferguson, 1988; Warn and Robert-Nicoud, 1990; Sandig and Kalnins, 1990; Jinguji and Ishikawa, 1992; and references within Conrad and Schroeder, 1990), future studies exploring a variety of systems should yield important information related to our expanding understanding of the mechanism of cytokinesis.

We wish to thank Dr. Fred Fay (Program in Molecular Medicine, University of Massachusetts Medical School, Worcester, MA) for helpful discussions, and members of the UMASS Biomedical Imaging Group, especially Mr. Doug Bowman for use of their scanning laser and digital microscopes to confirm observations made with our system. In addition, we extend special thanks to Mr. Long-guang Cao for helpful discussions, and Mr. John Silverman, Ms. Andrea Werme, and Ms. Beth Maynard, for help with the line drawings.

This work was supported by grants from the American Cancer Society PF-3758 (D. J. Fishkind) and National Institutes of Health, GM32476 (Y.-L. Wang).

Received for publication 10 May 1993 and in revised form 13 August 1993.

References

Agard, D. A. 1984. Optical sectioning microscopy: Cellular architecture in three dimensions. *Annu. Rev. Biophys. Bioeng.* 13:191–219.

Arnold, J. M. 1976. Cytokinesis in animal cells. *In* The Cell Surface in Animal Embryogenesis and Development. G. Poste and G. L. Nicolson, editors. Elsevier/North-Holland, New York. 55–88.

Aubin, J. E., K. Weber, and M. Osborn. 1979. Analysis of actin and microfilament-associated proteins in the mitotic spindle and cleavage furrow of PtK2 cells by immunofluorescence microscopy. *Exp. Cell Res.* 124:93–109.

Axelrod, D. 1989. Fluorescence polarization microscopy. *Methods Cell Biol.* 30:333–352.

Beams, H. W., and R. G. Kessel. 1976. Cytokinesis: A comparative study of cytoplasmic division in animal cells. *Am. Sci.* 64:279–290.

Bray, D., and J. G. White. 1988. Cortical flow in animal cells. *Science (Wash. DC).* 239:883–888.

Cao, L.-G., and Y.-L. Wang. 1990*a*. Mechanism of the formation of contractile ring in dividing cultured animal cells. I. Recruitment of preexisting actin filaments into the cleavage furrow. *J. Cell Biol.* 110:1089–1095.

Cao, L.-G., and Y.-L. Wang. 1990*b*. Mechanism of the formation of contractile ring in dividing cultured animal cells. II. Cortical movement of microinjected actin filaments. *J. Cell Biol.* 111:1905–1911.

Cao, L.-G., G. G. Babcock, P. A. Rubenstein, and Y.-L. Wang. 1992. Effects of profilin and profilactin on actin structure and function in living cells. *J. Cell Biol.* 117:1023–1029.

Castleman, K. R. 1979. Digital Image Processing. Prentice-Hall, Engelwood Cliffs, NJ. 429 pp.

Clark, S. W., and D. I. Meyer. 1992. Centractin is an actin homologue associated with the centrosome. *Nature (Lond.).* 359:246–250.

Conrad, G. W., and T. E. Schroeder, (editors). 1990. Cytokinesis: Mechanisms of Furrow Formation During Cell Division. vol. 582. Ann. N.Y. Acad. Sci. 325 pp.

Ferguson, D. J. P. 1988. An ultrastructural study of mitosis and cytokinesis in normal 'resting' human breast. *Cell Tissue Res.* 252:581–587.

Forer, A., and O. Benke. 1972. An actin-like component in spermatocytes of a crane fly (*Nephrotoma suturalis* Lowe). *Chromosoma (Berl.).* 39:145–173.

Fujiwara, K., and T. D. Pollard. 1976. Fluorescent antibody localization of myosin in the cytoplasm, cleavage furrow, and mitotic spindle of human cells. *J. Cell Biol.* 71:848–875.

Fujiwara, K., and T. D. Pollard. 1978. Simultaneous localization of myosin and tubulin in human tissue culture cells by double antibody staining. *J. Cell Biol.* 77:182–195.

Fukui, Y., and S. Inoué. 1991. Cell division in *Dictyostelium* with special emphasis on actomyosin organization in cytokinesis. *Cell Motil. Cytoskeleton.* 18:41–54.

Hai, C.-M., and B. Szeto. 1992. Agonist-induced myosin phosphorylation during isometric contraction and unloaded shortening in airway smooth muscle. *Am. J. Physiol.* 262:L53–L62.

Hird, S. N., and J. G. White. 1993. Cortical and cytoplasmic flow polarity in early embryonic cells of *Caenorhabditis elegans*. *J. Cell Biol.* 121:1343–1355.

Inoué, S. 1986. Video Microscopy. Plenum Press, New York. 584 pp.

Jinguji, Y., and H. Ishikawa. 1992. Electron microscopic observations on the maintenance of the tight junction during cell division in the epithelium of the mouse small intestine. *Cell Struct. Funct.* 17:27–37.

Kinoshita, K., Jr., H. Itoh, S. Ishiwata, K. Hirano, T. Nishizaka, and T. Hayakawa. 1991. Dual-view microscopy with a single camera: Real-time imaging of molecular orientations and calcium. *J. Cell Biol.* 115:61–73.

Kitanishi-Yumura, T., and Y. Fukui. 1989. Actomyosin organization during cytokinesis: reversible translocation and differential redistribution in *Dictyostelium*. *Cell Motil. Cytoskeleton.* 12:78–89.

LaFountain, J. R., Jr., M. A. Janicke, R. Balczon, and G. K. Richards. 1992. Cytochalasin induces abnormal anaphase in crane-fly spermatocytes and causes altered distribution of actin and centromeric antigens. *Chromosoma (Berl.).* 101:425–441.

Mabuchi, I. 1986. Biochemical aspects of cytokinesis. *Int. Rev. Cytol.* 101: 175–213.

Margolis, R. L., and P. R. Andreassen. 1993. The telophase disc: its possible role in mammalian cell cleavage. *BioEssays.* 15:201–207.

Maupin, P., and T. D. Pollard. 1986. Arrangement of actin filaments and myosin-like filaments in the contractile ring and of actin-like filaments in the mitotic spindle of dividing HeLa cells. *J. Ultrastruct. Mol. Struct. Res.* 94:92–103.

McDonald, K. 1984. Osmium ferricyanide fixation improves microfilament preservation and membrane visualization in a variety of animal cell types. *J. Ultrastruct. Res.* 86:107–118.

Mittal, B., J. M. Sanger, and J. W. Sanger. 1987. Visualization of myosin in the cytoplasm, cleavage furrow, and mitotic spindle of human cells. *J. Cell Biol.* 105:1753–1760.

Molè-Bajer, J., A. S. Bajer, and S. Inoué. 1988. Three-dimensional localization and redistribution of F-actin in higher plant mitosis and cell plate formation. *Cell Motil. Cytoskeleton.* 10:217–228.

Opas, J., and M. S. Soltynska. 1978. Reorganization of the cortical layer during cytokinesis in mouse blastomeres. *Exp. Cell Res.* 113:208–211.

Perry, M. M., H. A. John, and N. S. T. Thomas. 1971. Actin-like filaments in the cleavage furrow of the newt egg. *Exp. Cell Res.* 65:249–253.

Rappaport, R. 1986. Establishment of the mechanism of cytokinesis in animal cells. *Int. Rev. Cytol.* 105:245–281.

Rappaport, R. 1991. Cytokinesis. *In* Comparative Physiology: Oogenesis, Spermatogenesis, and Reproduction. Vol. 10. R. K. H. Kinne, editor. Karger, Basel. 1–36.

Rost, F. W. D. 1991. Quantitative fluorescence microscopy. Cambridge University Press, Cambridge, England. 236 pp.

Salmon, E. D. 1989. Cytokinesis in animal cells. *Curr. Opin. Cell Biol.* 1:541–547.

Sandig, M., and V. I. Kalnins. 1990. Reorganization of circumferential microfilament bundles in retinal epithelial cells during mitosis. *Cell Motil. Cytoskeleton.* 17:133–141.

Sanger, J. M. 1975. Presence of actin during chromosomal movement. *Proc. Natl. Acad. Sci. USA.* 72:2451–2455.

Sanger, J. M., and J. W. Sanger. 1980. Banding and polarity of actin filaments in interphase and cleaving cells. *J. Cell Biol.* 86:568–575.

Sanger, J. M., B. Mittal, J. S. Dome, and J. W. Sanger. 1989. Analysis of cell division using fluorescently labeled actin and myosin in living PtK2 cells. *Cell Motil. Cytoskeleton.* 14:201–219.

Satterwhite, L. L., and T. D. Pollard. 1992. Cytokinesis. *Curr. Opin. Cell Biol.* 4:43–52.

Schroeder, T. E. 1970. The contractile ring. I. Fine structure of dividing mammalian (HeLa) cells and the effects of cytochalasin B. *Z. Zellforsch. Mikrosk. Anat.* 109:431–449.

Schroeder, T. E. 1972. The contractile ring. II. Determining the brief existence, volumetric changes, and vital role in cleaving *Arbacia* eggs. *J. Cell Biol.* 53:419–434.

Schroeder, T. E. 1973. Actin in dividing cells: contractile ring filaments bind heavy meromyosin. *Proc. Natl. Acad. Sci. USA.* 70:1688–1692.

Shaw, P. J., and D. J. Rawlins. 1991. Three-dimensional fluorescence microscopy. *Prog. Biophys. Mol. Biol.* 56:187–213.

Skoufias, D. A., and J. M. Scholey. 1993. Cytoplasmic microtubule-based motor proteins. *Curr. Opin. Cell Biol.* 5:95–104.

Small, J. V. 1981. Organization of actin in the leading edge of cultured cells; Influence of osmium tetroxide and dehydration on the ultrastructure of actin meshworks. *J. Cell Biol.* 91:695–705.
Small, J. V., G. Rinnerthaler, and H. Hinssen. 1982. Organization of actin meshworks in cultured cells: the leading edge. *Cold Spring Harbor Symp. Quant. Biol.* 46:599–611.
Usui, N., and M. Yoneda. 1982. Ultrastructural basis of the tension increase in sea-urchin eggs prior to cytokinesis. *Dev. Growth & Differ.* 24:453–465.
Wang, Y.-L. 1984. Reorganization of actin filament bundles in living fibroblasts. *J. Cell Biol.* 99:1478–1485.
Warn, R. M., and M. Robert-Nicoud. 1990. F-actin organization during the cellularization of the *Drosophila* embryo as revealed with a confocal laser scanning microscope. *J. Cell Sci.* 96:35–42.
Yonemura, S., and S. Kinoshita. 1986. Actin filament organization in the sand dollar egg cortex. *Dev. Biol.* 115:171–183.
Yumura, S., H. Mori, and Y. Fukui. 1984. Localization of actin and myosin for the study of ameboid movement of *Dictyostelium* using improved immunofluorescence. *J. Cell Biol.* 99:894–899.
Zeligs, J. D., and S. H. Wollman. 1979. Mitosis in thyroid follicular epithelial cells *in vivo*. III. Cytokinesis. *J. Ultrastruct. Res.* 66:288–303.
Zeligs, J. D., and S. H. Wollman. 1981. Ultrastructure of cytokinesis in blood capillary endothelial cells in thyroid gland *in vivo*. *J. Ultrastruct. Res.* 75:291–299.